Activation and Deactivation of Au−Cu/SBA-15 Catalyst for Preferential Oxidation of CO in H$_2$-Rich Gas

Xu Li,[†] Stella See Soon Fang,[†] Jaclyn Teo,[†] Yong Lim Foo,[‡] Armando Borgna,[†] Ming Lin,*[,‡] and Ziyi Zhong*[,†]

[†]Institute of Chemical and Engineering Sciences, Agency for Science, Technology and Research (A*Star), 1 Pesek Road, Jurong Island, Singapore, 627833

[‡]Institute of Materials Research and Engineering, Agency for Science, Technology and Research (A*Star), 3 Research Link, Singapore 117602

S *Supporting Information*

ABSTRACT: This work aims to develop an efficient catalyst for preferential oxidation (PROX) of CO in a H$_2$-rich gas and obtain a clear structure−property relationship of the catalyst. A Au/CuO/SBA-15 catalyst was designed and prepared via a nanoengineering approach in which the metallic particles of average size 3 nm located in the vicinity of CuO particles were highly dispersed on the SBA-15 support. It was found that the CuO particles could reduce the gold (Au) particle size, stabilize the Au particles, and facilitate the activation of molecular oxygen. Although this catalyst is extremely active for the PROX reaction at room temperature and superior to the Au/SBA-15 and CuO/SBA-15 catalysts, it deactivates easily. Clear experimental evidence showed that CuO was reduced to Cu$_2$O and Cu in the reductive reaction gas mixture, and the Cu further combined/dissolved into the Au particles during the reaction. The alloying of Au and Cu not only decreased the catalytic activity of the Au particles but also reduced the ability of CuO to activate molecular oxygen. Fortunately, this alloying process could be reversed via a simple calcination in air to activate the catalyst. The identification of the catalyst structural evolution and this new contributing factor toward the deactivation of the Au catalysts has provided insights into the field of Au catalysis.

KEYWORDS: *gold catalyst, AuCu alloy, PROX reaction, particle size, point EDX analysis, activation, deactivation*
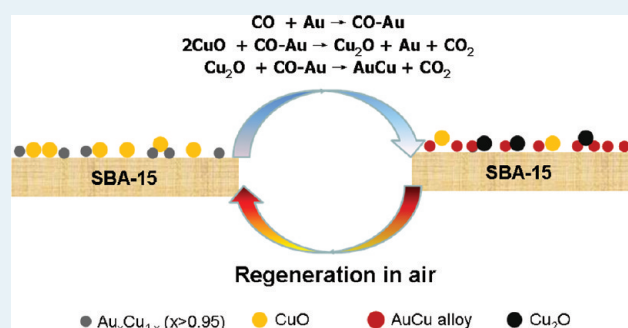
1. INTRODUCTION

Obtaining clear "structure−property" relationships for catalysts and thus establishing the groundwork for true rational design of heterogeneous catalysts are the key objectives in catalysis study.[1,2] In heterogeneous catalysis, various active sites often coexist in one catalyst. Their structures and performances depend not only on the bulk property of each catalyst component but also on local environmental parameters such as particle size, geometry, any presence of defects, as well as interactions among catalyst components, etc. Although in the past decade progress has been made in catalyst design and development with the application of novel nanoparticle synthetic methods, advanced analytical instrumentation and surface science techniques, and first-principles calculations,[2,3] most of these active sites and reaction mechanisms are still not well understood. In the late 1980s, Haruta et al.[4] first found that when gold (Au) particles in some supported Au catalysts were below 5 nm in size, they exhibited high catalytic activity in CO oxidation, altering the initial impression that Au was catalytically inert. Thereafter, this size-dependent catalytic property of Au catalysts was confirmed in a number of catalytic reactions.[5,6] Nevertheless, there are different opinions concerning the nature of the Au active sites; for example, whether such sites exist as positive, nonmetallic, or metallic Au atoms or whether certain defects are present.[7−12]

In addition, most Au catalysts still suffer from rapid deactivation, which is a big barrier to their practical applications. Their deactivation mechanism remains debated and is often attributed to the agglomeration of Au particles, CO$_2$ poisoning, the consumption of catalyst surface OH groups in a CO oxidation reaction, or the change of oxidation states, etc.[13−17] Fortunately, Au catalysis is usually applied under rather mild conditions, especially in CO oxidation, thus offering the convenience and feasibility to characterize these catalysts using advanced surface characterization techniques and enabling one to obtain deep understanding of the nature of the active sites and of the reaction/deactivation mechanism.

In catalyst preparation, nanoengineering often allows for much better control in particle size, composition, and local environments. Tsang et al.[18] decorated Pt particles with Co atoms and

achieved improved selectivity in α,β-unsatured aldehyde conversion to unsaturated alcohols because Co atoms could block unselective low coordination sites on Pt. To improve the sintering resistance of the Au particles, Dai et al.[19] successfully coated Au/TiO$_2$ surfaces with a thin SiO$_2$ layer that could anchor the active Au particles while maintaining their activity. Eichhorn et al.[2] covered Ru nanoparticles with a 1−2-monolayer-thick shell of Pt particles via a first-principles guided synthesis and achieved enhanced activity in preferential oxidation of CO in H$_2$-rich gas. We have noticed that Zhang and Mou's groups jointly worked on Au−Cu alloy particles supported on SBA-15, which exhibited a high activity in CO oxidation.[20,21] By comprehensively considering literature results, we anticipate that a good Au catalyst for CO oxidation should contain at least a small amount of cationic Au species[12] and a reducible catalyst support (MO$_x$) for molecular oxygen activation,[17,22] and the active Au/MOx particles should be accommodated in certain pores that allow full access of the reactant molecules while hindering particle agglomeration.

Here, we report the design and preparation of a highly dispersed Au/CuO/SBA-15 catalyst via a nanoengineering approach and the characterization of this catalyst at the atomic scale with high-resolution transmission electron microscopy (HRTEM), and high-angle annular dark field scanning TEM (HAADF-STEM) and some other in situ techniques. The SBA-15 support was first functionalized with a layer of 3-aminopropyltriethoxysilane (APTES) molecules bearing −NH$_2$ groups, which facilitated the dispersion of Au and CuO particles during their deposition and precipitation (DP) process. In the pretreatment process, instead of just reducing the as-prepared catalyst in H$_2$,[20,21] we further calcined the catalysts in air so as to generate as many nano Au particles and CuO particles as possible. The catalyst was tested in the low temperature preferential oxidation (PROX) reaction because it is an important industrial reaction used for purification of H$_2$ in hydrogen fuel cells.[23,24] Meanwhile, we made use of techniques such as HRTEM and HAADF-STEM to characterize the catalysts before and after the PROX reaction, which revealed the structural change of individual catalyst particles. For the first time, we have observed a reversible Cu phase migration and separation to and from the Au nanoparticles in the cycle of deactivation and regeneration, revealing that the alloying of Au and Cu components in this catalyst is the main reason for catalyst deactivation under a reducing atmosphere at low temperatures.

2. EXPERIMENTAL SECTION

2.1. Synthesis of Au/CuO/SBA-15, Au/SBA-15, and Cu/SBA-15 Catalysts.
Three catalysts—Au/CuO/SBA-15, Au/SBA-15, and Cu/SBA-15—with a theoretical loading of 3 wt % Au and 1 wt % Cu were prepared and tested. The APTES-functionalized SBA-15 was used as the catalyst support (see the Supporting Information), and the deposition of both Au and Cu was achieved at room temperature using the DP method.[13] In the DP process, HAuCl$_4$ and Cu(NO$_3$)$_2$ were used as the precursors, and the solution pH value was adjusted to ~9 with 0.1 M NaOH. The slurry was continuously stirred for 2 h. The precipitate was centrifuged and washed with DI water and then dried at room temperature in a vacuum oven. Au/SBA-15 and Cu/SBA-15 catalysts were prepared by the same method.

2.2. Characterization of Catalysts.
A catalytic test was carried out in a fixed-bed reactor: typically, 50 mg of catalysts, supported by quartz wools, was packed into a quartz tube. Prior to the reaction, a two-step pretreatment of the catalysts was carried out: (step 1) Reduction of the catalyst was done with 5% H$_2$ in Ar at a flow rate of 20 mL/min at 150 °C for 1 h. (step 2) After cooling down the catalyst, oxidation was then carried out under 20 mL/min of purified air at 400 °C for another 1 h to remove the organic residue in the catalyst and form the CuO phase. After the pretreatment, the catalyst was tested in a gas stream with a composition of 1% CO, 1% O$_2$, 18% CO$_2$, and 78% H$_2$ (this gas mixture imitated the real reformate composition and was purchased from National Oxygen Pte. Ltd., Singapore) at a GHSV of 20 000 h^{-1}. The reactants and products were analyzed online using a GC (Shimadzu-14B) equipped with both TCD and FID detectors. The following formulas give the calculation of the CO conversion and CO$_2$ selectivity:

$$\text{CO conversion (\%)} = 100 \times [\text{CO (inlet)} - \text{CO (outlet)}]/\text{CO (inlet)} \quad (1)$$

$$\text{CO}_2 \text{ selectivity (\%)} = 100 \times [\text{reacted CO/reacted O}_2] \quad (2)$$

The temperature-programmed reduction (TPR) measurements were performed on a Thermo TPD/R/O 1100. A 50 mg portion of each sample was pretreated in purified air at 300 °C for 1 h, cooled down in Ar gas, and then reduced with 5% H$_2$ from room temperature to 800 °C at a ramp rate of 10 °C/min. The in situ FT-IR measurement for CO adsorption (diffusion reflectance FT-IR, DRIFTS) was done in a DRIFT cell, which was embedded in an Excalibur Series FT-IR spectrometer. All samples were subjected to the two-step pretreatment process mentioned earlier in the DRIFT cell. Following the pretreatment, the samples were cooled down and then purged with Ar gas for 30 min before introducing 2.5% CO gas in Ar into the cell.

The solid UV−visible absorption spectrum was measured using a Shimadzu UV-3600 spectrophotometer equipped with three detectors: A PMT detector (photomultiplier tube) for the ultraviolet and visible regions and InGaAs and PbS detectors for the near-infrared region. A background reference was taken using barium sulfate before the measurements. Samples (10−20 mg) were pressed in the middle of a barium sulfate pellet in the sample holder and scanned in the range of 185−900 nm.

2.3. TEM Analysis and Electron Tomography of Catalysts.
TEM observations and 3D electron tomography were performed on a FEI Titan 80/300 S/TEM (scanning/transmission electron microscope) operated at an accelerating voltage of 200 kV. For TEM sample preparation, catalyst powders were dispersed in ethanol with the assistance of sonication, and one drop of the solution was dropped onto a carbon-coated TEM grid. The magnification of high-resolution TEM images was carefully calibrated by a standard Si sample. The lattice distances of catalysts were calculated using the fast Fourier transform of the image obtained with an error of 1% (0.002 nm). The HAADF-STEM images were constructed by collecting the electrons scattered to the high angles when the nanosized beam was scanned across the specimen. Since the phase and diffraction contrast is significantly suppressed in HAADF-STEM image and the intensity of the image is approximately proportional to the square atomic number (Z^2) of the scattering materials, one is able to discriminate the nanosized metallic particles from a thick oxide support due to a large Z difference between AuCu and silica SBA-15. The size distributions of metallic particles

were determined by a random selection of more than 100 particles from HAADF-STEM images for each sample.

The composition analysis of each metal particle was carried out using energy dispersive X-ray spectroscopy (EDX) at both TEM and STEM modes. Instead of Cu grids, Mo TEM grids were used to obtain accurate atomic ratios between Au and Cu. The specimen was tilted 10° toward the detector to minimize the blockage of TEM grid bars to X-ray emissions. In the STEM mode, the probing size of the converged beam was between 0.2 and 0.3 nm, and beam spot size 6 was selected to obtain a better signal-to-noise ratio. The acquisition time for each spectrum was 15 s.

For electron tomography, a total of 70 HAADF-STEM images were collected with a tilt range of −64° to 74°, at 2° incremental steps. The stage tilting and image acquisition were done automatically by the FEI Xplore-3D tomography program, and the tracking and refocusing of the sample area were carried out manually to shorten the total acquisition time and minimize beam damage to the sample. The magnification of the STEM images was 180 000 times, corresponding to 0.70 nm per pixel. The acquisition time for one 1024 × 1024 sized image was 20 s. The final tilt series data were aligned using a cross-correlation method and reconstructed by a simultaneous iterative reconstruction technique (50 iterations) using Inspect3D, and the reconstructed 3D volume was visualized by voxel rendering and orthogonal slices using Amira 4.1. The resolution of the reconstructed tomogram was about 1 nm.[25]

3. RESULTS

3.1. Catalytic Evaluation of Catalysts. Figure 1 illustrates the catalytic performance of the Au/CuO/SBA-15 catalyst at different reaction conditions. At room temperature (Figure 1a), the CO conversion reaches almost 100% on Au/CuO/SBA-15 (the lowest CO concentration on Au/CuO/SBA-15 at GHSV = 20 000 h^{-1} is close to 2 ppm), 59% on Au/SBA-15, and 0.2% on CuO/SBA-15 (the results not shown here for the latter two catalysts). However, this Au/CuO/SBA-15 catalyst deactivates easily. After a 3 h reaction, the CO conversion starts to decline, and after ~8 h, only ~20% conversion is achieved. Figure 1b shows the catalytic performance at various reaction temperatures. The CO conversion always decreases with an increase in reaction temperature. At 150 °C, only 15% conversion is achieved. It can be observed that the decrease in CO conversion with reaction temperature is parallel to the decrease in the CO_2 selectivity, whereas the O_2 conversion remains high and similar above 50 °C (Figure 1b). This indicates that the competing H_2 oxidation becomes obvious at higher reaction temperatures. The accumulation effect due to previous stages, as the temperature is raised, is negligible because a temperature-dependent CO conversion profile (Figure S1 of the Supporting Information) done from 150 to 25 °C coincides closely with that from 25 to 150 °C (Figure 1b). In addition, the catalyst also shows thermal deactivation when it is heated to 100 °C (Figure S2 of the Supporting Information).

The catalytic activity at room temperature measured at a higher GHSV of 40 000 h^{-1} dropped from 55% to 26%, after the catalyst was heated to 100 °C for a brief period. Figure 1c shows the effect of various regeneration methods on the catalytic performance. After deactivation, the catalyst can be regenerated via a calcination step in air at 300 °C. Meanwhile, treatments both in H_2 and in CO lead to lower catalytic activities. It should be noted that the second round of regeneration in air only partially recovers the catalytic activity. To prove that the
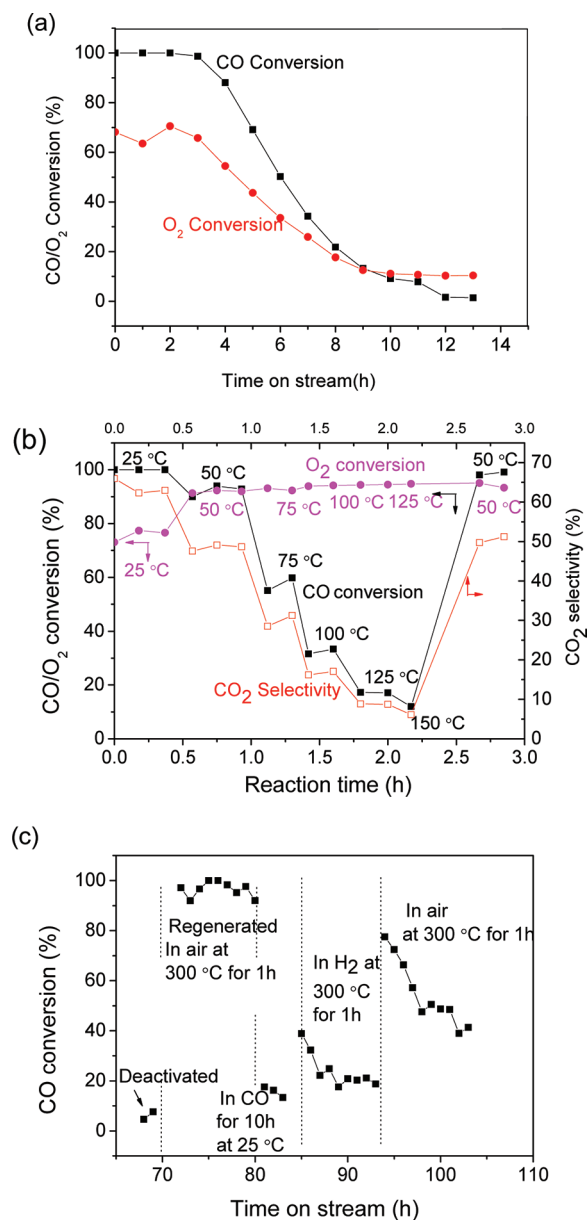

Figure 1. Catalytic performance profiles of the Au−Cu/SBA-15 catalyst at GHSV = 20 000 h^{-1}: (a) time-dependent CO conversion at room temperature, (b) temperature-dependent CO oxidation on the same catalyst, and (c) after various regeneration treatments. The CO_2 selectivity is also shown in part b.

oxidation treatment in the pretreatment of the catalyst is necessary for generating a highly active catalyst, the catalyst was further reduced by 5% H_2/Ar at 400 °C for 1 h after the 2-step pretreatment (Figure S3 of the Supporting Information). The result shows a significant drop in the initial CO conversion at room temperature from 100% to 70% for the reduced catalyst, indicating that the reduction treatment at 400 °C leads to a lower catalytic activity.

3.2. Structural Analysis of Au/CuO/SBA-15 Catalysts. To understand the "structure-catalytic property" relationship, the size, morphology, composition, chemical states, and catalytic effectiveness of the Au/CuO/SBA-15, Au/SBA-15, and Cu/SBA-15 catalysts were carefully studied by various techniques, including HRTEM, HAADF-STEM, electron tomography, UV−vis, TPR, and DRIFTS. Figure 2 shows the XRD patterns of the
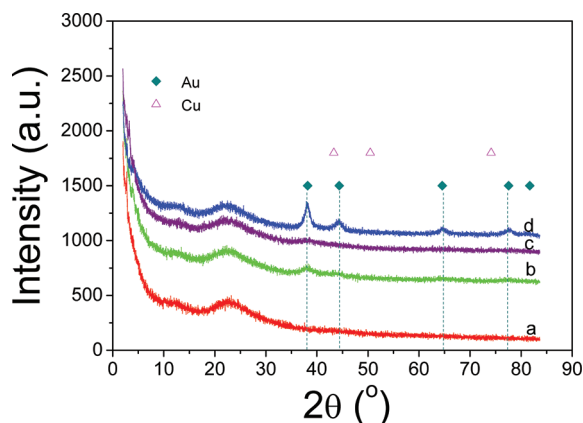
Figure 2. XRD patterns of the Au−Cu/SBA-15 samples (a) dried and before reaction, (b) after calcination at 200 °C for 1 h, (c) after pretreatment in H₂ for 1 h at 150 °C and oxidation in air for 1 h at 400 °C, and (d) after reaction at 100 °C for 10 h. For comparison, standard XRD patterns of Au and Cu are indicated by diamonds and triangles.

Figure 3. (a) HAADF-STEM image of the Au/CuO/SBA-15 catalyst after the activation; (b) corresponding 3D visualization; (c) an *x-y* slice showing that the metallic particles are mostly anchored inside the pore channels; (d) HRTEM image of metallic particles; (e) histogram of particle size distribution derived from 330 particles; and (f) atomic percentage of Cu in 33 metallic particles showing most particles are either pure Au or Au-dominant AuCu alloy.

Au/CuO/SBA-15 catalyst after being activated using the two-step pretreatment process. No peaks related to Au, Cu, or CuO are observed, indicating low loading of the metal precursors or very small particle size. However, after a direct calcination in air only at 200 °C for 1 h or after reaction at 100 °C for 10 h, diffraction peaks of metallic Au particles appear in the Au/CuO/SBA-15 catalyst, indicating the growth of the Au particles. TEM measurements show that the average Au particle size is 3.7 nm in the former (Supporting Information, Figure S4) and much bigger in the latter.

The HAADF-STEM image of the Au/CuO/SBA-15 catalyst in Figure 3a shows that nanosized metallic particles are uniformly dispersed on the mesoporous support. The mean metallic particle size is 3.0 nm with a standard deviation of 30% (Figure 3e), indicating a narrow size distribution. It is noted that the average metal particle size in Au/CuO/SBA-15 is smaller than that in Au/SBA-15 (3.7 nm, as shown in Figure 4a), suggesting that the introduction of the Cu phase facilitates the higher dispersion of smaller Au particles. To identify the locations of the supported metallic particles, electron tomography was used to present a 3-dimensional (3D) visualization. The 3D volume reconstructed by HAADF-STEM tomography reveals a relatively homogeneous distribution of metallic particles across the porous supports, as shown in Figure 3b and in a movie in the Supporting Information. An *x−y* slice, shown in Figure 3c and taken from the middle of the mesoporous support with a thickness of 0.7 nm, further supports that the metal particles are, indeed, located inside the channels of the mesoporous SBA-15 support rather than on the external surface of the support.

The actual loading of elemental Au to Cu onto the mesoporous support in Au/CuO/SBA-15 measured by EDX is around 85:15 by weight ratio, lower than the precursor ratio of 3:1 used in the synthesis. This suggests a limited loading of Cu on the SBA-15 support and a particle composition that is different from the theoretical loading. Copper is an element that is easily oxidized into Cu₂O or CuO by oxygen at high temperatures. The detailed structural analysis of Cu/SBA-15 reveals that no metallic Cu nanoparticles were formed after having gone through the 2-step pretreatment process.

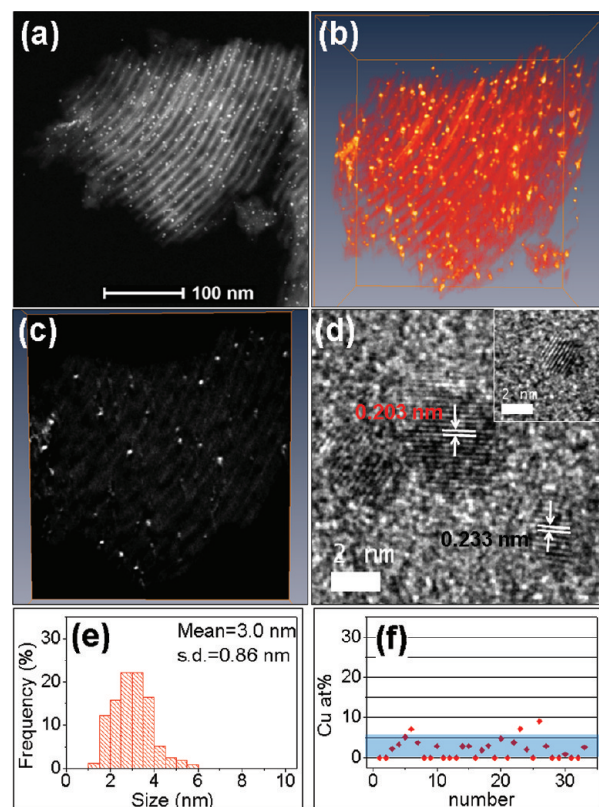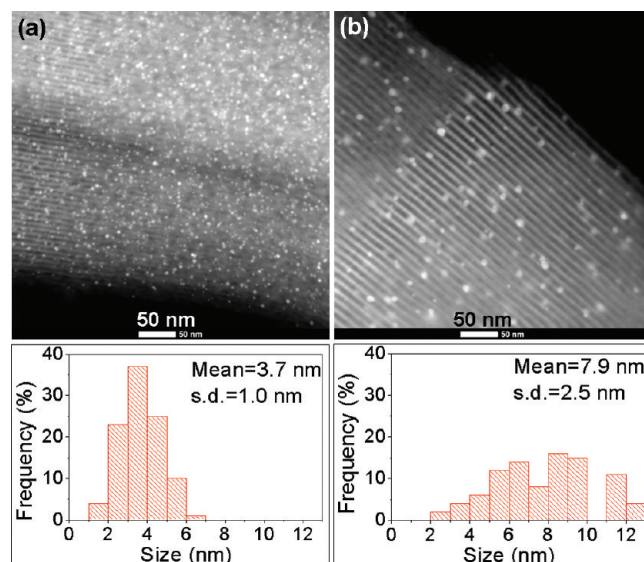Figure 5 shows the typical TEM and STEM images of the Cu/SBA-15 catalyst, in which the mesoporous channels are

Figure 4. STEM image of 3% Au/SBA-15 (a) before and (b) after the catalytic reaction at room temperature for 24 h.

quite "smooth". We did not observe any nucleation of Cu related particles on the surface, probably because of the low contrast between the oxide particles and the thick SBA-15 support (from hundred of nanometers to several micrometers thick). However, corresponding EDX spectra taken from the mesoporous
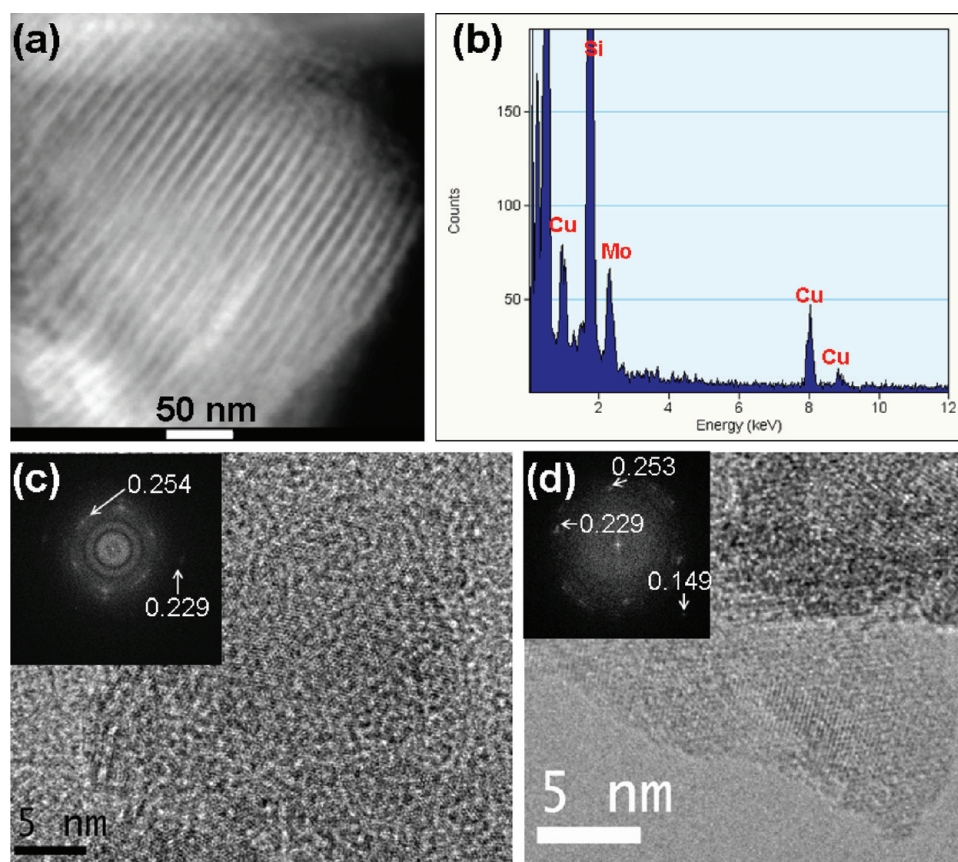
Figure 5. TEM analysis of CuO/SBA-15 catalyst after activation. (a) HAADF-STEM image; (b) EDX spectrum of the corresponding area (Mo TEM grid); (c, d) two HRTEM images with the corresponding FFT images shown in the inset.

supports confirmed the presence of Cu element on the support almost everywhere, without any other impurities being detected. Although the thick SBA-15 support makes it difficult to obtain clear observation of the structures using TEM, some crystalline materials at the edge of SBA-15 in HRTEM images are still spotted. The lattice spacings measured in Figure 5c are 0.254 and 0.229 nm, and that in Figure 5d measured 0.253, 0.229, and 0.149 nm, respectively. The lattice distances measured from HRTEM images agree well with that of crystalline CuO (JCPDS 48−1548), which have spacings of 0.253, 0.252, 0.232, and 0.150 nm for {11−1}, {002}, {111}, and {113} planes, respectively. This confirms that no metallic Cu nanoparticles are formed in the Cu/SBA-15 catalysts after reduction and further oxidation at 400 °C in air. Instead, highly dispersed and crystalline CuO is observed on the surface of the SBA-15 support as a result of the oxidation of Cu phase, resulting in the composition of CuO/SBA-15 catalyst.

Formation of CuO is also expected on the Au/CuO/SBA-15 catalyst, which underwent the same pretreatment. However, it is difficult to accurately determine the composition of individual metallic particles on the mesoporous support due to the overlapping copper signals originating from the CuO that is widely supported on the substrate. To remove the background Cu (from CuO) signals from the substrate, we have conducted a point EDX analysis by selecting individual metallic particles on the carbon membrane. These individual particles were separated from the mesoporous support by ultrasound sonication during the TEM sample preparation. Thirty-three individual metallic particles were analyzed, and it is found that most of the

particles are either pure Au or AuCu alloys with <5 at. % of Cu inside, as shown in Figure 3f.

The HRTEM image in Figure 3d revealed the particles have single crystalline structures with a discernible lattice spacing of 0.203 and 0.233 nm, which is close to the spacings of 0.205 nm for Au {100} and 0.236 nm for Au {111} planes, further supporting that the metal particles are either pure gold or an alloy of AuCu containing a very low content of Cu. Thus, the actual composition of formed Au/CuO/SBA-15 catalyst is Au_xCu_{1-x}/CuO/SBA-15 ($x > 0.95$), with the CuO phase being located either between Au and SBA-15 or highly dispersed on SBA-15 (Figure 5). For simplicity, hereafter, we will still state the catalyst as Au/CuO/SBA-15 unless specially mentioned otherwise. It is worth noting that stronger interaction between Au and CuO than that between Au and SBA-15 is naturally expected.

3.3. Structural Evolution of Au/CuO/SBA-15 Catalysts after Deactivation and Regeneration. Figure 6 and Figure S5 of the Supporting Information show the STEM and HRTEM images of the Au/CuO/SBA-15 catalyst after deactivation (reacted at room temperature for 13 h) and after the first regeneration in air at 300 °C respectively. For the deactivated and regenerated samples, their average particle size is 3.1 nm, slightly different from the size of the fresh catalyst before reaction (3 nm). In the deactivated catalyst, it is interesting to note that some CuO particles were reduced to Cu_2O, as determined by the lattice fringes of 0.247 nm, which corresponds to the {111} planes of Cu_2O in Figure 6c. On the other hand, in the regenerated catalyst, only CuO is detected, indicating the partial reduction of CuO in the PROX reaction even
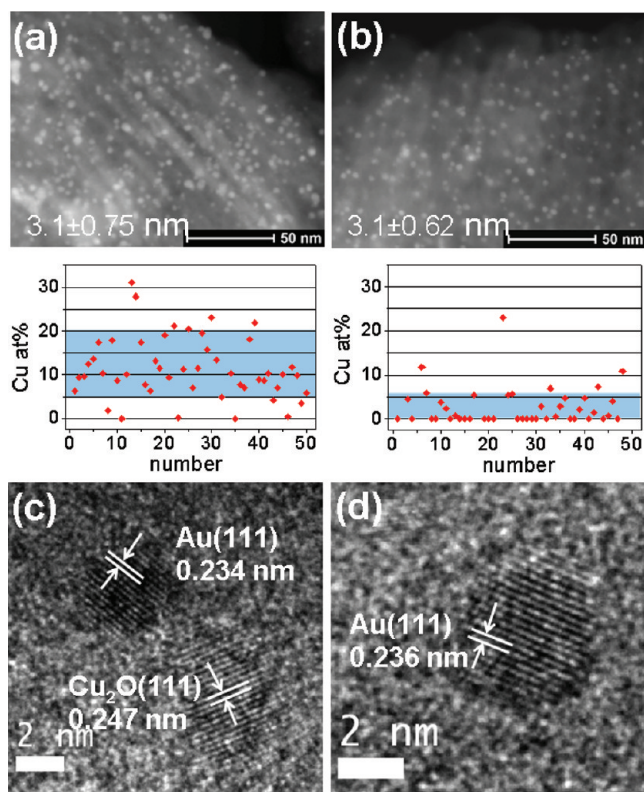
Figure 6. STEM and HRTEM images of the Au/CuO/SBA-15 catalyst: (a, c) deactivated catalysts after reaction at room temperature for 24 h and (b, d) regenerated catalysts at 300 °C in air. The graphs between a and c and b and d show the measured composition of the individual metallic particles.

at room temperature, and the reoxidation of Cu_2O in the regeneration.

The main difference in the activated, deactivated, and regenerated catalysts lies in the composition of metallic particles (Au/Cu ratio) measured via point EDX analysis. Comparing the graph in Figure 3f and the graphs between a and c and b and d in Figure 6, it is clearly seen that the freshly activated catalyst has a low Cu content in the Au_xCu_{1-x} metallic particles ($x > 0.95$), whereas the deactivated catalyst has a much higher Cu content ($0.95 > x > 0.8$). After the regeneration, the Cu content in the Au_xCu_{1-x} particles decreased again ($x > 0.95$). Assuming a linear relationship between the lattice constant and the composition of alloy, we can determine the composition in the alloy using Vegard's law,[26] an alternative method with which the lattice parameter of Au_xCu_{1-x} alloy can be estimated by using the formula $a_{AuCu-alloy} = xa_{Au} + (1-x)a_{Cu}$. The lattice spacing of Au_xCu_{1-x} ($0.95 > x > 0.8$) particles in the deactivated catalyst is measured at 0.234 nm in Figure 6c.

Ten other HRTEM images of the AuCu alloy particles were depicted in Figure S6 in the Supporting Information. The lattice spacings of AuCu alloy {111} planes were measured between 0.231 and 0.236 nm, corresponding to a Cu content of 17 (0.231 nm), 13 (0.232 nm), 9 (0.233 nm), and 6 at. % (0.234 nm) in the Au_xCu_{1-x} alloy. This is in good agreement with the measurement from single particles using EDX, in which the molar percentage of Au in the Au_xCu_{1-x} alloy particles after reaction ranged between 80% and 95%. However, the Vegard's law is only approximately valid for those binary materials with small difference in lattice parameter and bulk crystals.

A larger deviation to the Vegard's law is expected in nanoparticles as a result of the lattice relaxation on the surface, making the change in lattice distance smaller with a low concentration of copper. Since the HRTEM image is subjected to instrumental error of 1% or 0.002 nm, it is also difficult to differentiate the small difference in lattice spacing of alloy nanoparticles with a lower percentage of copper in the alloy. Thus, it is more reliable to determine the metallic particle composition by both localized EDX analysis of individual particles and lattice calculation. Correlating this with the catalytic performance, it can be concluded that pure Au particles or Au_xCu_{1-x} alloy with a low fraction of Cu are highly active for CO oxidation and that alloying of Au with more Cu leads to the deactivation. Obviously, a Cu phase migration into Au metallic particles has occurred during the PROX reaction at room temperature, and it is reversed in the regeneration process because of the oxidation of Cu in the alloy.

In addition to the atomic and localized analysis using TEM, the catalysts were further characterized by other techniques to provide statistical evidence for the above hypothesis. Figure 7
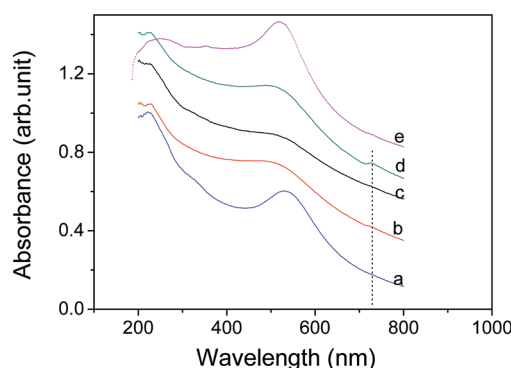

Figure 7. UV−vis spectra for Au−Cu/SBA-15 catalysts experienced with various treatments: (a) catalysts calcined in air at 200 °C for 1 h, (b) after activation (reduced in H_2 at 150 °C then oxidized at 400 °C in air), (c) after reaction at room temperature for 13 h, (d) regenerated in air, and (e) Au/SBA-15 catalysts after reaction.

shows the UV−vis spectra measured for Au/CuO/SBA-15 and CuO/SBA-15 catalysts after various treatments and after the PROX reaction at room temperature. A sharp absorbance peak near 530 nm is observed for the Au/CuO/SBA-15 catalyst calcined at 200 °C in air (see Figure 7). For the activated catalyst that underwent through the two-step pretreatment process, the absorption occurs at 510 nm, indicating a much smaller metal particle size and a higher dispersion,[27] although it was calcined at a higher temperature. This result is in agreement with XRD measurement (Figure 2). Likewise, after the PROX reaction, small Au_xCu_{1-x} particles are still present, as supported by the weak absorbance peak near 510 nm. However, after the regeneration, in addition to the weak absorbance peak at around 510 nm, a new peak at ∼730 nm also appears, indicating the additional formation of large CuO particles,[28] which should have a negative influence on the catalytic performance of the catalyst. Clearly, one of the roles of the regeneration is to recover the CuO phase in the catalyst. For the Au/SBA-15 catalyst, after the reaction at room temperature for 24 h, a sharp absorption peak is observed (Figure 7e), indicating an increase in the Au particle size. Thus, it is clear that CuO can maintain and stabilize the high dispersion of small Au particles on the catalyst support, which is understandable because CuO has a

much stronger interaction with Au particles than the SBA-15 surface (silica).

Figure 8 presents the TPR profiles of the three catalysts. These reduction peaks reflect the reduction behavior of the metal oxides
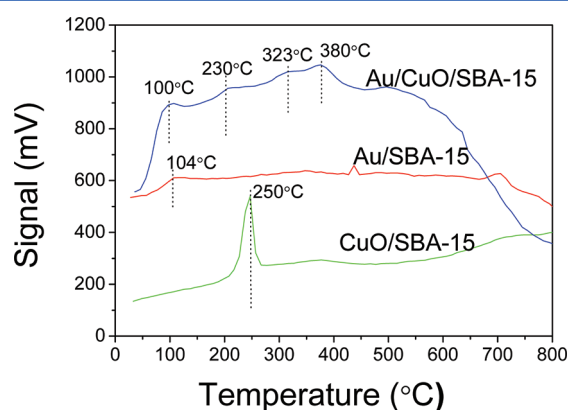

Figure 8. TPR profiles of various catalysts after the activation.

or the reactivity of the active oxygen species associated with the metal ions toward H_2. The lower the reduction peak temperature, the higher the reactivity. The Au/SBA-15 catalyst has a weak reduction peak at 104 °C, indicating a very high reactivity of the active oxygen species associated with the Au cation (AuO_δ).[29] For the CuO/SBA-15 sample, the observation of a single reduction peak at 250 °C indicates that the reduction of CuO to metallic Cu is a one-step reaction and that there is a much lower reactivity of the activity oxygen species toward H_2 in CuO than that in AuO_δ.

In the Au/CuO/SBA-15 catalyst, the intensity of the low reduction peak at 100 °C is much higher than that of the Au/SBA-15 catalyst. Three new peaks at 230, 323, and 380 °C are observed, indicating a multistep reduction process of CuO ($CuO \rightarrow Cu_2O \rightarrow Cu$) as well as the heterogeneity of the catalyst surface. The appearance of Cu_2O phase is also confirmed by TEM observation. Kim et al.[30] has performed a systematic study on the reduction behaviors of CuO using 5% H_2 in He and found that with sufficient H_2, CuO could be reduced to metallic Cu in one step, and with insufficient H_2, Cu_2O could be formed as an intermediate.

The reduction of CuO is easier than that of Cu_2O. Previously we have proved using in situ TG-FT-IR technique that the deposition of nanosized Au particles on α-Fe_2O_3 support led to the generation of a larger amount of active oxygen than pure α-Fe_2O_3, and these active oxygen species could easily react with CO in low reaction temperatures.[31] The significantly increased active oxygen amount on the Au/CuO/SBA-15 catalyst (top curve in Figure 8) could be attributed to a synergetic effect between the two components. In the TPR experiment, a rapid consumption of H_2 was expected by the increased amount of active oxygen species, leading to a lack of sufficient H_2 for CuO reduction, thus causing the formation of Cu_2O species. The detailed interaction between Au and CuO should be further investigated in the future.

The Au/CuO/SBA-15 catalyst was also tested for PROX reaction at high temperature. Figure 9 shows the TEM result for the catalyst before and after the reaction at 100 °C. After the reaction, the most significant change in the catalyst is the formation of linear Au or Au−Cu nanoparticles due to a higher surface diffusion rate of the metals, indicating the mobility of the nanoparticles in the SBA-15 channels. A similar phenomenon was observed for the catalyst of Pt deposited on FSM-16 in a CO/H_2O mixture.[32] The agglomeration of Au particles
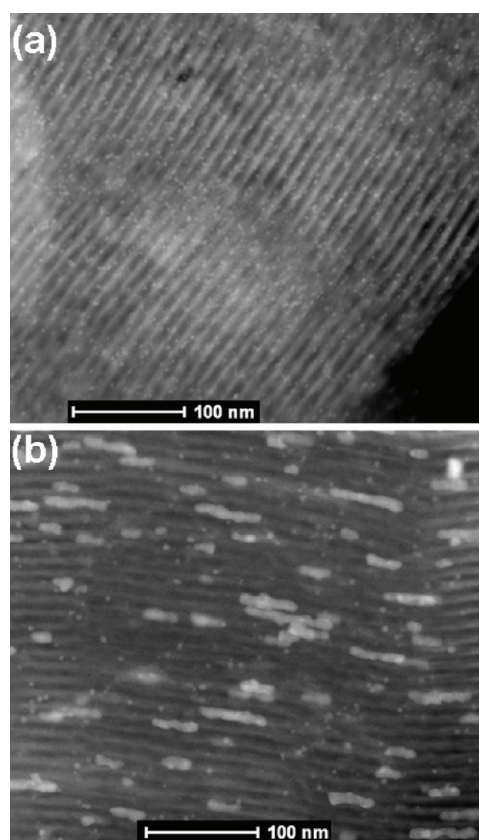

Figure 9. TEM analysis of the Au/CuO/SBA-15 catalyst before and after reaction at 100 °C for 5 h: (a) before the reaction and (b) after the reaction.

is detrimental and will have a negative impact on their catalytic activity.

The DRIFTS results measured at 30 and 150 °C, respectively, for the Au/CuO/SBA-15, CuO/SBA-15, and Au/SBA-15 catalysts are presented in Figure S7 of the Supporting Information. Comparing the spectra during CO adsorption at 30 °C, CO molecules absorbed on metallic Au (2000−2031 cm^{-1}) and on cationic CuOx or AuO$_y$ (2100−2171 cm^{-1}) are always identified for the three catalysts.[31−35] However, upon a closer look at the changes in the absorbance peak intensity near 2000 and 2100 cm^{-1} (Figure S7A, C, and E of the Supporting Information), it can be concluded that the Au component should be mainly in the form of metallic Au, and any cationic Au species are difficult to identify because even for the Au/SBA-15 catalyst (Figure S7E of the Supporting Information), there is almost no change in the absorbance between 2100 and 2200 cm^{-1} after the CO absorption. Probably only a trace amount of cationic Au species exists at the interface, if there is any.

For the FT-IR spectra measured at 150 °C, the overall CO absorbance becomes very weak in the whole range. Meanwhile, there are no obvious changes in the OH group absorbance (3500−4000 cm^{-1}) after the CO introduction. In contrast, a peak near 1640 cm^{-1} is always observed for the spectra measured at 30 °C, which can be assigned to the existence of moisture. Considering the fact that a H_2-rich gas is used in our PROX reaction, a competitive oxidation of H_2 always exists (see Figure 1b, oxygen selectivity is always less than 100%), which can generate a trace amount of H_2O. Thus, it is reasonable to assume that there should be no lack of surface OH groups on

our catalysts during the PROX reaction. In addition, comparing with the IR spectra on the catalyst before CO adsorption, no obvious surface carbonate accumulation ($1600-1700$ cm^{-1}) is observed, probably because of the acidic property of the silica surface.

4. DISCUSSION

On the basis of the above results, we have proposed the following mechanism to explain the activation and deactivation of catalysts. During the synthesis process, the Au and Cu precursors are homogeneously mixed and precipitated on the mesoporous support. Subsequently, nanosized Cu, Au, or AuCu alloy particles are formed by the H$_2$ reduction in step 1 of the pretreatment process. The single-phase Cu and Cu in the AuCu alloy is then oxidized to CuO particles on the substrate in step 2 of the pretreatment process, resulting in the formation of Au or Au dominant Au$_x$Cu$_{1-x}$ nanoparticles and highly dispersed CuO on mesoporous substrates. The addition of Cu in the AuCu alloy in step 1 pretreatment can also generate active Au/CuO or Au$_x$Cu$_{1-x}$/CuO catalysts with smaller Au or Au$_x$Cu$_{1-x}$ size (3.0 nm as compared with 3.7 nm for the Au/SBA-15 catalyst) due to the depletion and oxidation of the Cu fraction into CuO, where the as-generated CuO are attached to the Au or Au$_x$Cu$_{1-x}$ metallic particles. The formation of well-mixed Au−Cu particles in step 1 pretreatment is important to the nucleation of nanosized Au particles (3 nm). After the oxidation, Au can be segregated from the alloy into small-sized particles and generates stronger interaction with CuO. The direct calcination of the pristine catalysts only led to the nucleation of bigger Au particles (3.7 nm) as a result of the nano diffusion of free Au species, which has already been confirmed by XRD (Figure 2b and Figure S4 of the Supporting Information). It is noted that the size of Au particles after 200 °C calcination (3.7 ± 0.92 nm) is similar to that of the pure Au/SBA-15 sample (3.7 ± 1.0 nm), further indicating the importance of Au−CuO interaction for the synthesis of nanocatalysts. Without the formation of the AuCu alloy during step 1 pretreatment, the diffusion and nucleation behavior of Au on AuCu/SBA-15 is almost the same as that in the Au/SBA-15 catalyst. Thus, the 2-step pretreatment process plays an important role in activating the Au/CuO/SBA-15 ($x > 0.95$) catalyst.

Sra et al.[36] found that from room temperature to 175 °C, Cu can diffuse into Au to form an atomically disordered solid solution Cu$_x$Au$_{1-x}$. The ordered AuCu and AuCu$_3$ start to be nucleated at 200 and 300 °C, respectively. At 400 °C, these ordered alloy structures start to decompose or become disordered, and by 500 °C, the solid solution will be completely dealloyed to metallic Au and some Cu$_2$O by reacting with trace oxygen. In our synthesis process, the structural evolution from AuCu/SBA-15 (formed after the H$_2$ reduction in the catalyst activation) to Au$_x$Cu$_{1-x}$/CuO/SBA-15 (formed after oxidation in air in the catalyst activation) agrees well with Sra's findings, except that the Cu can be fully oxidized to CuO in air at low temperature (400 °C).

Our TEM results showed that there is almost no change for the Au particle size in the Au/CuO/SBA-15 catalyst after the PROX reaction for 13 h at room temperature. The average particle size of the catalyst before the reaction, after the reaction, and after the regeneration is 3.0 ± 0.86, 3.1 ± 0.75, and 3.1 ± 0.62 nm, respectively. The decreasing standard deviation of particle size after reaction is caused by the decrease in particles smaller than 2 nm. The percentage of particles with a diameter of <2 nm decreases from 13.2% before reaction

to <5.2% after reaction, resulting in the narrower size distribution after the reaction. Nonetheless, even with a similar size range obtained after the regeneration, the catalytic performance of particles can still be recovered by 90%. This suggests that the diminishing of the particles smaller than 2 nm has only a minor impact on the catalytic properties. Furthermore, in comparison with the 3% Au/SBA-15 catalysts, in which the average size has increased from 3.7 to 7.9 nm, the addition of Cu in the catalyst significantly hinders the aggregation and growth of the Au particles due to the alloying process and strong interaction between metallic Au or Au$_x$Cu$_{1-x}$ and CuO.

However, a significant change in Au$_x$Cu$_{1-x}$ particle composition did occur after the reaction at room temperature and after the regeneration. After the reaction, the Cu content in Au$_x$Cu$_{1-x}$ particles was significantly increased, but it was reverted back to the initial level after subsequent regeneration. No CuO or Cu$_2$O shells on the outside of Au particles were observed under TEM. Instead, an almost pure metallic phase was still observed after the reaction. As known, Au−Cu can form a solid solution and various ordered structures, such as AuCu, AuCu$_3$, and Au$_3$Cu, depending on Au/Cu ratio and treatment conditions. In our case, the Cu content increment in Au$_x$Cu$_{1-x}$ particles after the PROX reaction test at room temperature indicates that CuO was reduced to Cu$_2$O or even metallic Cu, and the latter either further combined with the Au$_x$Cu$_{1-x}$ particles or dissolved in them, and x changes from larger than 0.95 to between 0.8 and 0.95. From the aspects of oxygen activation and stabilization of Au particles, this reduction behavior of the CuO phase to Cu$_2$O and Cu is not beneficial to obtaining a high catalytic activity. Correlating with the catalytic performance, it is thus concluded that this further alloying process actually causes the deactivation of the catalysts at low reaction temperatures. At high temperatures ($\geq$100 °C), the Au$_x$Cu$_{1-x}$ particles become mobile in the CO gas, thus growing into bigger particles, which becomes another dominant factor that leads to the deactivation. The formation of these linear aggregates confirms that most of the Au particles are distributed inside the channels of SBA-15, as observed by electron tomography (Figure 3).

In other words, the most active catalyst configuration is that of Au/CuO/SBA-15, which consists of very small Au or Au$_x$Cu$_{1-x}$ particles in the immediate vicinity of CuO particles, with both of them being highly dispersed on SBA-15. This explains why in both catalyst activation and regeneration, the oxidation treatment process is always necessary to keep the catalyst active, as it can regenerate the CuO phase and reverse the alloying of the Au−Cu particles. This is also proven in Figure S3B of the Supporting Information, where the catalyst was subjected to a 400 °C reduction treatment after the two-step pretreatment, and a significant drop in catalytic activity was observed. The structural changes of the catalyst and the reaction mechanism are summarized and schematized in Figure 10.

Recently, Liu et al.[20] reported that for Au$_3$Cu$_1$/SiO$_2$ catalyst, the most active phase for CO oxidation was a Au core decorated with tiny Cu$_2$O patches. The Au core could adsorb CO molecules, and the Cu$_2$O phase could supply active oxygen. A similar phenomenon was observed by Dai et al.,[37] who had started from an AuCu/SiO$_2$ alloy catalyst, but concluded that the active catalyst was Au−CuO$_x$/SiO$_2$ after various treatments. In retrospect, these results support our conclusion that the most active phase is neither the Au−Cu alloy nor their solid solution, but the Au/CuO combination. The roles of the metal oxide layer in CO oxidation have been proposed by
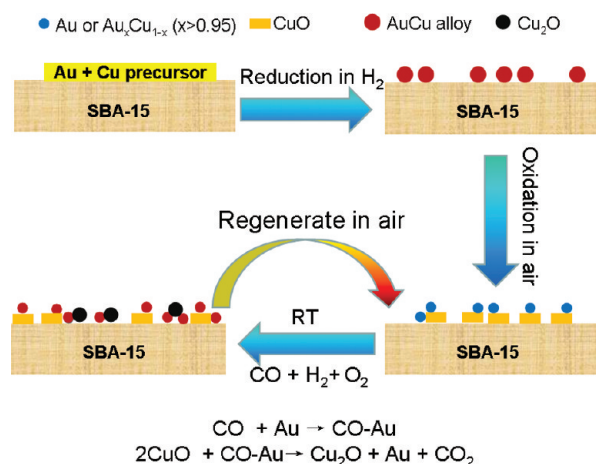
Figure 10. Catalyst structural evolution and reaction/deactivation mechanism.

Nieuwenhuys et al.,[38] who believed that in the $Au/MO_x/Al_2O_3$ systems (M=Cr, Mn, Fe, Co, Ni, Cu and Zn), CO molecules are adsorbed on Au particles or at the Au/MO_x perimeter and then oxidized by the active O donated by MO_x. Liu et al.[39] proved the existence of two kinds of active sites in supported Pt and Pd on FeOx catalysts. One is the Pt or Pd site for CO activation, and the other is the FeOx for oxygen activation. Zheng et al.[17] proposed that OH groups near oxygen vacancies in the TiO_2 supports are also involved in the oxygen activation. Although further clarification of the pathways for molecular oxygen activation is needed, clearly, it is related to the metal oxide support.

This $Au\text{-}CuO/SBA\text{-}15$ system is quite complicated and the interference from the SBA-15 support and low loadings of the metal components make it more difficult for some in situ characterizations. We are currently conducting experiments on AuCu model catalysts using in situ TEM and in situ XPS. Their results are expected to validate our predictions in this work and address some other critical issues of the AuCu catalyst used in PROX reaction, such as the nucleation process of alloy particles and oxidation state of Cu during PROX reactions.

CONCLUSION

In summary, we have successfully prepared an $Au/CuO/SBA\text{-}15$ catalyst via a nanoengineering approach. This includes the surface modification of SBA-15 with APTES molecules and the DP method for Au and Cu deposition. A two-step pretreatment process, which generates an active phase consisting of very small Au or Au_xCu_{1-x} particles in the immediate vicinity of highly dispersed CuO layer on SBA-15, results in a highly active catalyst for the PROX reaction. Three roles have been identified for the CuO layer: (i) minimizing the Au particle size and (ii) stabilizing them and (iii) facilitating the activation of molecular oxygen.

This metal–oxide biparticle structure is highly active for PROX reaction. It is found to be superior to both the Au/SBA-15 and the CuO/SBA-15 catalysts. However, this type of catalyst deactivates easily at both room temperature and high reaction temperatures, because CuO is reduced to Cu_2O and Cu under the reducing atmosphere, and the Cu phase further migrates to Au particles and combine/dissolve in them. Although we cannot exclude that some other factors may also lead to the deactivation of the catalysts, for example, the growth of the Au particles; however, in the early stage of the reaction at low temperatures, the main reason for the deactivation of the

catalyst is due to the alloying of Au and Cu. This alloying process can be reversed via the oxidation treatment process. At high reaction temperatures (≥ 100 °C), in addition to the combination of Au with Cu, the agglomeration of Au particles also needs to be suppressed to prevent the deactivation of the catalyst. We believe these fundamental findings will play an important role in new catalyst design and development as well as deepen our understanding of the catalytic behaviors.

ASSOCIATED CONTENT

Ⓢ Supporting Information

Description for the synthesis of SBA-15 and modification of the SBA-15 surface with 3-aminopropyltriethoxysilane (APTES); CO and O_2 conversion, CO_2 selectivity of Au/CuO/SBA-15 catalyst tested from 150 to 25 °C and from 25 to 150 °C; CO, O_2 conversion and CO_2 selectivity of Au/CuO/SBA-15 catalyst at a higher GHSV of 40 000 h^{-1}; comparison of CO and O_2 conversion for catalyst treated after two-step pretreatment and after two-step pretreatment and a third 400 °C reduction; STEM image of AuCu/SBA-15 catalysts directly calcined in air at 200 °C for 1 h; TEM study of Au/CuO/SBA-15 catalyst after pretreatment, after reaction at room temperature for 24 h, and after regeneration in air at 300 °C; typical HRTEM images of AuCu nanoparticles after PROX reaction; DRIFTS results. A video clip is provided to show the 3D structures of the distribution of metal particles on SBA-15 after segmentation. This information is available free of charge via the Internet at http://pubs.acs.org

AUTHOR INFORMATION

Corresponding Author

*(M.L.) Fax: 65-67744657. E-mail: m-lin@imre.a-star.edu.sg. (Z.Z.) Fax: 65-83166182. E-mail: zhong_ziyi@ices.a-star.edu.sg.

Notes

The authors declare no competing financial interest.

REFERENCES

(1) Besenmacher, F.; Chorkendorff, I.; Clausen, B. S.; Hammer, B.; Molenbroek, A. M.; Nørskov, J. K.; Stensgaard, I. *Science* **1998**, *279*, 1913−1915.

(2) Alayoglu, S.; Nilekar, A. U.; Mavrikakis, M.; Eichhorn, B. *Nat. Mater.* **2008**, *7*, 333−338.

(3) Green, I. X.; Tang, W.; Neurock, M.; Yates, J. T., Jr. *Science* **2011**, *333*, 736−739.

(4) Haruta, M.; Kobayashi, T.; Sano, H.; Yamada, N. *Chem. Lett.* **1987**, *16*, 405−408.

(5) Kung, M. C.; Davis, R. J.; Kung, H. H. *J. Phys. Chem. C* **2007**, *111*, 11767−11775.

(6) Corma, A.; Serna, P. *Science* **2006**, *313*, 332−334.

(7) Herzing, A. A.; Kiely, C. J.; Carley, A. F.; Landon, P.; Hutchings, G. J. *Science* **2008**, *321*, 1331−1335.

(8) Qi, C.; Huang, J.; Bao, S.; Su, H.; Akita, T.; Haruta, M. *J. Catal.* **2011**, *281*, 12−20.

(9) Enache, D. I.; Edwards, J. K.; Landon, P.; Solsona-Espriu, B.; Carley, A. F.; Herzing, A. A.; Watanabe, M.; Kiely, C. J.; Knight, D. W.; Hutchings, G. J. *Science* **2006**, *311*, 362−365.

(10) Valden, M.; Lai, X.; Goodman, D. W. *Science* **1998**, *281*, 1647−1650.

(11) Guzman, J.; Carretin, S.; Corma, A. *J. Am. Chem. Soc.* **2005**, *127*, 3286−3287.

(12) Min., B. K.; Friend, C. M. *Chem. Rev.* **2007**, *107*, 2709−2724.

(13) Haruta, M.; Tsubota, S.; Kobayashi, T.; Kageyama, H.; Genet, M. J.; Delmon, B. *J. Catal.* **1993**, *144*, 175−192.

(14) Costello, C. K.; Yang, J. H.; Law, H. Y.; Wang, Y.; Lin, J. N.; Marks, L. D.; Kung, M. C.; Kung, H. H. *Appl. Catal., A* **2003**, *243*, 15−24.

(15) Zhong, Z.; Lin, J. Y.; Teh, S. P.; Teo, J.; Dautzenberg, F. M. *Adv. Funct. Mater.* **2007**, *17*, 1402−1408.

(16) Ng, J. W. D.; Zhong, Z.; Luo, J.; Borgna, A. *Int. J. Hydrogen Energy* **2010**, *35*, 12724−12732.

(17) Zheng, Z. F.; Teo, J.; Chen, X.; Liu, H. W.; Yuan, Y.; Waclawik, E. R.; Zhong, Z.; Zhu, H. Y. *Chem.—Eur. J.* **2010**, *16*, 1202−1211.

(18) (a) Tsang, S. C.; Cailuo, N.; Oduro, W.; Kong, A. T. S.; Clifton, L.; Yu, K. M. K.; Thiebaut, B.; Cookson, J.; Bishop, P. *ACS Nano* **2008**, *2*, 3544−3551. (b) Tan, H. R.; Tan, L.; Boothroyd, K. M. K.; Hansen, B.; Foo, J.; Lin, P. *J. Phys. Chem. C* **2012**, *116*, 242−247.

(19) Ma, Z.; Brown, S.; Howe, J. Y.; Overbury, S. H.; Dai, S. *J. Phys. Chem. C* **2008**, *112*, 9448−9457.

(20) Liu, X.; Wang, A.; Wang, X.; Mou, C. Y.; Zhang, T. *Chem. Commun.* **2008**, 3187−3189.

(21) Liu, X.; Wang, A.; Li, L.; Zhang, T.; Mou, C. Y.; Lee, J. F. *J. Catal.* **2011**, *278*, 288−296.

(22) Schubert, M. M.; Hackenberg, S.; van Veen, A. C.; Muhler, M.; Plzak, V.; Behm, R. J. *J. Catal.* **2001**, *197*, 113−122.

(23) Kahlich, M. J.; Gasteiger, H. A.; Behm, R. J. *J. Catal.* **1997**, *171*, 93−105.

(24) Marino, F.; Descorme, C.; Duprez, D. *Appl. Catal., B* **2004**, *54*, 59−66.

(25) (a) Tan, J. P. Y; Tan, H. R.; Boothroyd, C.; Foo, Y. L.; He, C. B.; Lin, M. *J. Phys. Chem. C* **2012**, *116*, 3544−3551. (b) Tan, H. R.; Tan, J. P. Y; Boothroyd, C.; Hansen, T. W.; Foo, Y. L.; Lin, M. *J. Phys. Chem. C* **2012**, *116*, 242−247.

(26) Denton, R.; Ashcroft, N. W. *Phys. Rev. A* **1991**, *43*, 3161−3164.

(27) Zhong, Z.; Patskovskyy, S.; Bouvrette, P.; Luong, J. H. T.; Gedanken, A. *J. Phys. Chem. B* **2004**, *108*, 4046−4052.

(28) Marion, M. C.; Garbowski, E.; Primet, M. *J. Chem. Soc. Faraday Trans.* **1991**, *87*, 1795−1800.

(29) Khoudiakov, M.; Gupta, M. C.; Deevi, S. *Appl. Catal., A* **2005**, *291*, 151−161.

(30) Kim., J. Y.; Rodriguez, J. A.; Hanson, J. C.; Frenkel, A. I.; Lee, P. L. *J. Am. Chem. Soc.* **2003**, *125*, 10684−10692.

(31) Zhong, Z.; Highfield, J.; Lin, M.; Teo, J.; Han, Y. F. *Langmuir* **2008**, *24*, 8576−8582.

(32) Mohamed, M. M.; Thabet, M. *J. Phys. Chem. C* **2008**, *112*, 8890−8897.

(33) Demri, D.; Hindermann, J. P.; Diagne, C.; Kiennemann, A. *J. Chem. Soc., Faraday Trans.* **1994**, *90*, 501−506.

(34) Zhong, Z.; Ang, H.; Choong, C.; Chen, L.; Huang, L.; Lin, J. *Phys. Chem. Chem. Phys.* **2009**, *11*, 872−880.

(35) Perkas, N.; Teo, J.; Shen, S.; Wang, Z.; Highfield, J.; Zhong, Z.; Gedanken, A. *Phys. Chem. Chem. Phys.* **2011**, *13*, 15690−15698.

(36) Sra, A. K.; Schaak, R. E. *J. Am. Chem. Soc.* **2004**, *126*, 6667−6672.

(37) Bauer, J. C.; Mullins, D.; Li, M. J.; Wu, Z.; Payzant, E. A.; Overbury, S. H.; Dai, S. *Phys. Chem. Chem. Phys.* **2011**, *13*, 2571−2581.

(38) Grisel, R. J. H.; Nieuwenhuys, B. E. *Catal. Today* **2001**, *64*, 69−81.

(39) Liu, L.; Zhou, F.; Wang, L.; Qi, X.; Shi, F.; Deng, Y. *J. Catal.* **2010**, *274*, 1−10.